Int. J. Therm. Sci. (2000) 39, 1–17

S1290-0729(00)00199-9/FLA

Numerical investigation of bubble coalescence characteristics under nucleate boiling condition by a lattice-Boltzmann model

Zhi Lin Yang *, T.N. Dinh, R.R. Nourgaliev, B.R. Sehgal

Division of Nuclear Power Safety, Royal Institute of Technology, Drottning Kristinas väg 33A, 10044 Stockholm, Sweden

(Received 12 March 1999, accepted 21 May 1999)

Abstract — A numerical study was performed to investigate the characteristics of bubble growth, detachment and coalescence on vertical, horizontal, and inclined downward-facing surfaces. The FlowLab code, which is based on a lattice-Boltzmann model of two-phase flows, was employed. Macroscopic properties, such as surface tension (σ) and contact angle (β), were implemented through the fluid–fluid (G_σ) and fluid–solid (G_t) interaction potentials. The model predicted a linear relationship between the macroscopic properties (σ, β) and microscopic parameters (G_σ, G_t). The simulation results on bubble departure diameter appear to have the same parametric dependence as the empirical correlation. Hydrodynamic aspects of bubble coalescence are investigated by simulating the growth and detachment behavior of multiple bubbles generated on horizontal, vertical, and inclined downward-facing surfaces. For the case of horizontal surface, three distinct regimes of bubble coalescence were represented in the lattice-Boltzmann simulation: lateral coalescence of bubbles situated on the surface; vertical coalescence of bubbles detached in a sequence from a site; and lateral coalescence of bubbles, detached from the surface. Multiple coalescence was predicted on the vertical surface as the bubble detached from a lower elevation merges with the bubble forming on a higher site. The bubble behavior on the inclined downward-facing surface was represented quite similar to that in the nucleate boiling regime on a downward-facing surface. © 2000 Éditions scientifiques et médicales Elsevier SAS

two-phase flow / nucleate boiling / bubble coalescence / lattice-Boltzmann

Nomenclature

A	constant	
B	dimension of space	
b	number of velocity vectors	
D	nondimensional bubble diameter	
d_0	arbitary constant	
$\boldsymbol{e}, c$	lattice speed	$\mathrm{m\cdot s^{-1}}$
f, n	density distribution function	
F	force	$\mathrm{kg\cdot m\cdot s^{-2}}$
G	interaction strength	
g	nondimensional gravity acceleration, body force	
L	nondimensional distance between two bubble generation sites	
m	molecular weight of component	$\mathrm{kg\cdot mol^{-1}}$
P	pressure	$\mathrm{kg\cdot m^{-1}\cdot s^{-2}}$
Q	nondimensional flow rate	
S	the number of phase	
t	nondimensional time	
$\boldsymbol{u}$	velocity vector, (u_1, u_2, u_3)	$\mathrm{m\cdot s^{-1}}$
v	nondimensional velocity	
V	volume	$\mathrm{m^3}$
W	interaction potential	
$\boldsymbol{x}$	coordinates, (x_1, x_2, x_3)	m

Greek symbols

α	inclination angle of heater surface	degree
β	contact angle	degree
ν	kinematic viscosity	$\mathrm{m^2\cdot s^{-1}}$
ρ	density	$\mathrm{kg\cdot m^{-3}}$
τ	relaxation time	$\mathrm{s^{-1}}$
ψ	effective number density	

Subscripts

a	index of discrete lattice velocity direction
b	the number of the discrete
S	the number of phases
σ	interaction potential

* Corespondence and reprints.
yang@ne.kth.se

t fluid–solid interaction

Superscripts

eq equilibrium
j index of phase

1. INTRODUCTION

Boiling mechanisms and boiling heat transfer crisis play an important role in the performance of power generation equipment, in which evaporation of a coolant is utilized to achieve high heat removal rate. Nucleate boiling is the major boiling mode in normal operation. In contrast, a transition to a film boiling would significantly decrease the heat transfer through low-conductivity vapor layer.

In the nucleate boiling regime, several mechanisms were identified to govern heat transfer from the heated surface to the coolant. Namely, transient conduction in the bubble growth zone, evaporation at the vapor–liquid interface, liquid natural convection in the vicinity of the growing bubble and at a distance from it (single-phase circulation). The relative role of these mechanisms in the boiling heat transfer varies with the boiling conditions. At higher heat fluxes, evaporation is the dominant mode in the fully developed nucleate boiling. In particular, the nucleation site density is increased with the increase of heat flux or wall temperature.

Clearly, physics of nucleate boiling and boiling heat transfer crisis is governed by dynamics of the vapor structure [1], namely, isolated bubble regime, coalescing bubbles and vapor mushrooms (*figure 1*). It was found that a transition from partial to fully developed nucleate boiling is associated with merging of uprising bubbles in the vertical direction and of neighboring bubbles on the horizontal surface. More importantly, at heat fluxes well above the first transition value, the surface becomes covered with large vapor mushrooms, which significantly reduce the heated area available for liquid cooling. Further coalescence of vapor structures leads to departure from nucleate boiling to boiling crisis.

Intensive investigations of boiling heat transfer crisis have been conducted for the last 40 years. The objective of the research was to develop a plausible physical and mathematical model which enables generalization of the data base on critical heat fluxes (CHF) for reliable predictions of CHF in various flow, pressure and geometry conditions. Several fruitful approaches were proposed and a number of models were developed and validated (see [2] for a comprehensive review). It should be noted, however, that the physical picture and assumptions on which these models were based were quite different. In any case, the phenomena of bubble merging and coalescence are believed to govern the boiling dynamics at high heat fluxes and have a profound effect on the initiation of the boiling crisis. Current understanding of the bubble coalescence is however limited due to difficulties in local and instantaneous measurements of thermal hydraulic parameters in the vicinity of the merging bubbles and vapor structure.

In the present work, an advanced flow-modeling method, namely lattice-Boltzmann (LB) equation method, is employed to perform numerical investigation of the bubble growth and detachment behavior, and the bubble coalescence under different nucleate boiling conditions. Focus is placed on regimes of the bubble coalescence and the effect of the flow-surface configuration on the bubble coalescence dynamics.

2. THE LATTICE-BOLTZMANN METHOD

2.1. Introduction to lattice-Boltzmann method

The lattice-Boltzmann (LB) method [3] has been developed quite recently. As an extension of the lattice gas automata (LGA), the LB method describes macroscopic complex flows by dealing with the underlying micro-world. It has important advantages over its ancestor, LGA. First, the white noise of the LGA model, coming from statistical nature of the automata, is eliminated in the LB method. Second, the LB method can overcome two physical artifacts of the original LGA, i.e. the lack of Galilean invariance, and the velocity-dependent pressure term. The LB method recovers the Navier–Stokes equations in the incompressible flow limit. The LB method has proved to be competitive with the traditional CFD (computational fluid dynamics) methods. Moreover, since the LB method can be considered as a mesoscopic approach, lying in between microscopic molecular dynamics and conventional macroscopic fluid dynamics, it can be useful when microscopic statistics and macroscopic description of flow are important, e.g., in problems involving surface tension, capillarity and phase transition in multiphase multicomponent systems.

2.2. Model formulation

The idea of the lattice-Boltzmann approach originates from kinetic theory of gases, according to which, the

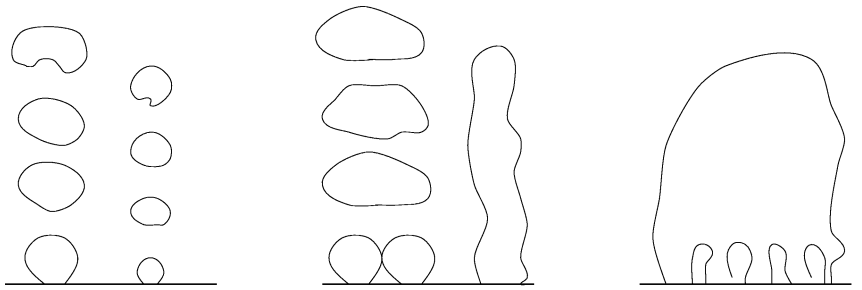

Figure 1. Gaertner's [1] identification of vapor structures in nucleate boiling.

dynamics of flow is described by an integro-differential Boltzmann equation:

$$\frac{\partial f}{\partial t} + \boldsymbol{u} \cdot \nabla f = \sum(\boldsymbol{x}, \boldsymbol{u}, t) \tag{1}$$

where $\boldsymbol{x}$ and $\boldsymbol{u}$ are vectors of three-dimensional space coordinator and velocity, respectively, t is time, $f(\boldsymbol{x}, \boldsymbol{u}, t)$ is the density distribution function, which represents a density of particles inside an infinitesimal volume, $\Delta V = \Delta x_i \Delta u_i$, of 6D phase space $(u_i, x_i,\ i = 1, 3)$. The right-hand side of the Boltzmann equation (1) is a collision integral, which describes the source/sink of particles (due to collision) in the infinitesimal volume ΔV. The simplest model for the collision integral, which is valid in the case of small deviation of the system from the equilibrium state, has the following form:

$$\sum(\boldsymbol{x}, \boldsymbol{u}, t) = -\frac{1}{\tau}\left(f - f^{\mathrm{eq}}\right) \tag{2}$$

where τ has the meaning of relaxation (towards equilibrium) time, f^{eq} is the equilibrium density distribution. Typically, Maxwell–Boltzmann equilibrium distribution is employed.

In the lattice-Boltzmann approach, an analog of Boltzmann equation (1) is solved on a regular lattice, which fills the physical space under consideration. *Figure 2* shows the typical two-dimensional nine-speed (D2Q9) lattice scheme. In the lattice-Boltzmann method, the following conditions are employed:

- particle populations f may move only with discrete velocities $\boldsymbol{e}_a$. The corresponding populations are denoted by $n_a,\ a = 0, \ldots, b$;
- to redistribute populations f, a single relaxation time operator (equation (2)) is applied;

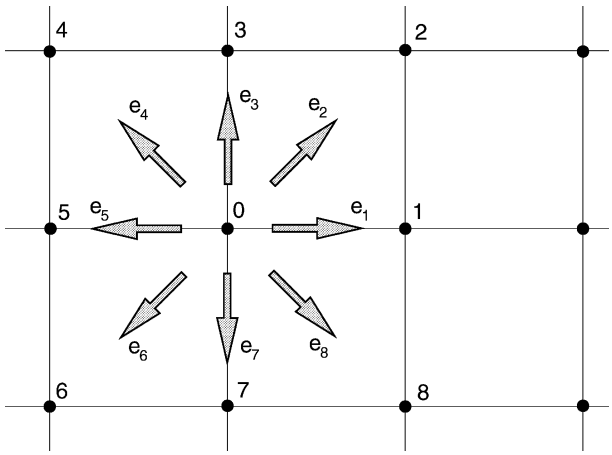

Figure 2. Lattice geometry and velocity vectors of D2Q9 model.

- the equilibrium velocity distribution function is written as a truncated power series of the macroscopic flow velocity.

The discrete-velocity-Boltzmann equation for multicomponent and multiphase flow is written in the form of the Boltzmann equation (1) [4]:

$$n_a^j(\boldsymbol{x} + \boldsymbol{e}_a, t+1) - n_a^j(\boldsymbol{x}, t) = -\frac{1}{\tau}\left[n_a^j(\boldsymbol{x}, t) - n_a^{j(\mathrm{eq})}(\boldsymbol{x}, t)\right] \tag{3}$$

where $n_a^{j(\mathrm{eq})}(\boldsymbol{x}, t)$ is the equilibrium distribution at $(\boldsymbol{x}, t)$, superscript j denotes the fluid component, $j = 1, \ldots, S$, and subscript a indicates the lattice velocity direction, $a = 0, \ldots, b$. We should note that equation (3) is normalized by the lattice spacing, Δx, and the reference lattice speed, $c = \Delta x / \Delta t$.

The functional form for the equilibrium distribution is chosen as

$$n_0^{j(\mathrm{eq})}(\boldsymbol{x}) = n^j(\boldsymbol{x})\left[d_0 - \frac{1}{c^2}\boldsymbol{u}^2\right] \tag{4}$$

$$n_a^{j(\mathrm{eq})}(\boldsymbol{x}) = n^j(\boldsymbol{x})\left[\frac{1-d_0}{b} + \frac{B}{c^2 b}\boldsymbol{e}_a\cdot\boldsymbol{u} + \frac{B(B+2)}{2c^4 b}\boldsymbol{e}_a\boldsymbol{e}_a:\boldsymbol{u}\boldsymbol{u} - \frac{B}{2bc^2}\boldsymbol{u}^2\right] \quad \text{for } a = 1,\ldots,b \tag{5}$$

where $n^j = \sum_{a=1}^{b} n_a^j$, d_0 is an arbitary constant, B is the dimension of space, c is the reference lattice speed, $\boldsymbol{e}_a\boldsymbol{e}_a:\boldsymbol{u}\boldsymbol{u} = (\boldsymbol{e}_a\cdot\boldsymbol{u})(\boldsymbol{e}_a\cdot\boldsymbol{u})$. The above form of LB equations is developed for the two-dimensional hexogonal ($b = 6$) and four-dimensional face-centered-hyper-cube (FCHC) ($b = 24$) lattices. Following Qian et al. [3], the four-dimensional FCHC lattice can be projected into two dimensions, resulting in a rectangular D2Q9 (2D and nine-speed) model. The dimensionless equilibrium equations (4) and (5) for the D2Q9 lattice model are, then, transformed into

$$n_0^{j(\mathrm{eq})}(\boldsymbol{x}) = A_0 n^j(\boldsymbol{x})\left[1 - \frac{3}{2}\boldsymbol{u}^2\right] \tag{6}$$

$$n_a^{j(\mathrm{eq})}(\boldsymbol{x}) = A_a n^j(\boldsymbol{x})\left[1 + 3\boldsymbol{e}_a\cdot\boldsymbol{u} + \frac{3}{2}\left(3\boldsymbol{e}_a\boldsymbol{e}_a:\boldsymbol{u}\boldsymbol{u} - \boldsymbol{u}^2\right)\right] \quad \text{for } a = 1,\ldots,b \tag{7}$$

where $A_0 = 4/9$ (the rest populations), if $a = 2, 4, 6$ and 8, $A_a = 1/9$, and if $a = 1, 3, 5$ and 7, $A_a = 1/36$. In the above expressions, the arbitrary constant d_0 in equations (4) and (5) was chosen as $1/3$ [5].

Physical quantities of flow, such as fluid density $\rho^j(\boldsymbol{x}, t)$ and fluid velocity $\boldsymbol{u}^j$, can be obtained from

$$\rho^j(\boldsymbol{x}, t) = \sum_a m^j n_a^j(\boldsymbol{x}, t) \tag{8}$$

$$\rho^j(\boldsymbol{x}, t)\boldsymbol{u}^j(\boldsymbol{x}, t) = m^j \sum_a n_a^j(\boldsymbol{x}, t)\boldsymbol{e}_a \tag{9}$$

where m^j is the molecular mass of the jth component.

As it has been shown analytically by Shan and Chen [4], the above choice of the equilibrium distribution functions and fluid velocity enables each of components to obey the isothermal Navier–Stokes equations with an ideal gas equation of state.

2.2.1. Interaction potential

Shan and Chen [4] proposed to introduce nonlocal interactions among the particles, in order to simulate the equation of state for a non-ideal gas. The interaction potential $W(\boldsymbol{x}, \boldsymbol{x}')$ is defined as

$$W(\boldsymbol{x}, \boldsymbol{x}') = G_{jj'}\psi^j(\boldsymbol{x})\psi^{j'}(\boldsymbol{x}') \tag{10}$$

where ψ^j is a function of $n(\boldsymbol{x})$ and plays the role of the effective number density for component j. $G_{jj'}$ is the interaction intensity. If only nearest-neighbor interactions are involved, the rate of change of momentum at each site is simply

$$\frac{\mathrm{d}P^j}{\mathrm{d}t} = -\psi^j \sum_{j'}^{S} G_{jj'} \sum_{a=0}^{b} \psi^{j'}(\boldsymbol{x} + \boldsymbol{e}_a)\boldsymbol{e}_a \tag{11}$$

where P is the pressure.

As shown in [4], with the above definition of the interaction potential, the equation of state can be written as

$$P = \frac{c^2}{B}\left[\sum_j (1-d_0)\rho^j + \frac{b}{2}\sum_{jj'} G_{jj'}\psi^j\psi^{j'}\right] \tag{12}$$

where the first term on the right-hand side is a kinetic contribution, while the second term is a contribution due to the inter-particle interaction. With interaction potential properly chosen, any equation of state can be modeled.

It is straightforward to introduce external body force as

$$\frac{\mathrm{d}P^j}{\mathrm{d}t}(\boldsymbol{x}) + \boldsymbol{g}^j\rho^j$$

where P and $\boldsymbol{g}$ are pressure and body force (or gravity). In such a case, after a collision, the new net momentum at site $\boldsymbol{x}$ for the jth component becomes

$$\rho^j(\boldsymbol{x})\boldsymbol{u}'^j(\boldsymbol{x}) = \rho^j(\boldsymbol{x})\boldsymbol{u}^j(\boldsymbol{x}) + \tau^j\left[\frac{\mathrm{d}P^j}{\mathrm{d}t}(\boldsymbol{x}) + \rho^j\boldsymbol{g}^j\right] \tag{13}$$

where $\boldsymbol{u}'^j$ is the new velocity used in equations (6) and (7).

2.2.2. Fluid–solid interaction

Martys and Chen [5] proposed to introduce the interaction force to describe the interaction between a fluid and a wall, which is defined as

$$F^j(\boldsymbol{x}) = -n^j(\boldsymbol{x}) \sum_a G_t^j s(\boldsymbol{x} + \boldsymbol{e}_a)(\boldsymbol{e}_a) \tag{14}$$

where $s = 0$ or 1 for a pore or a solid, respectively. By adjusting the interaction strength G_t^j (positive for

nonwetting fluid and negative for wetting fluid) for each fluid, one can control which fluid wets a surface preferentially.

Applying the Chapman–Enskog expansion procedure to the lattice-Boltzmann equation (3), one obtains the following mass and momentum equations for the fluid mixture treated as a single fluid [6]:

$$\frac{\partial \rho}{\partial t} + \nabla \rho \boldsymbol{u} = 0 \tag{15}$$

$$\frac{\partial \boldsymbol{u}}{\partial t} + \boldsymbol{u}\nabla \boldsymbol{u} = -\frac{\nabla P}{\rho} + \sum_{j=1}^{S} x^j \boldsymbol{g}^j + \nu \nabla^2 \boldsymbol{u} \tag{16}$$

where $\rho = \sum_{j=1}^{S} \rho^j$ is the total density of the fluid mixture, $x^j = \rho^j/\rho$ is the mass fraction of the component j. The kinematic viscosity of fluid can be obtained from

$$\nu = c^2 \frac{\sum_j^S x^j \tau^j - 1/2}{B+2} \tag{17}$$

where τ is the relaxation time in the LB equation. By choosing proper τ, the viscosity of fluid can be obtained.

2.2.3. Two-dimensional nine-speed D2Q9 lattice

Two-dimensional nine-speed D2Q9 lattice is employed in the present study. The $\boldsymbol{e}_a$, the nine discrete velocities, are defined by

$$\boldsymbol{e}_a = \begin{cases} 0, & a = 0 \\ c\left(\cos\frac{(a-1)\pi}{4}, \sin\frac{(a-1)\pi}{4}\right), & a = 1,3,5,7 \\ \sqrt{2}c\left(\cos\left[\frac{(a-2)\pi}{4} + \frac{\pi}{4}\right], \sin\left[\frac{(a-2)\pi}{4} + \frac{\pi}{4}\right]\right), & a = 2,4,6,8 \end{cases} \tag{18}$$

The lattice geometry and discrete velocities are shown in *figure 2*.

Care must be taken while projecting from the four-dimensional FCHC lattice to the two-dimensional D2Q9 model, since the interaction potential, equation (11), is different for these two lattices. In this case,

$$\frac{\mathrm{d}P^j}{\mathrm{d}t} = -\psi^j \sum_{j'}^{S} \sum_{a=0}^{b} G^a_{jj'} \psi^{j'}(\boldsymbol{x} + \boldsymbol{e}_a)\boldsymbol{e}_a \tag{19}$$

$$G^a_{jj'} = \begin{cases} 4G_\sigma & \text{for } |\boldsymbol{e}_a| = 1 \cdot c,\ a = 1,3,5,7 \\ G_\sigma & \text{for } |\boldsymbol{e}_a| = \sqrt{2} \cdot c,\ a = 2,4,6,8 \\ 0 & \text{otherwise} \end{cases}$$

where G_σ is a constant of interaction potential.

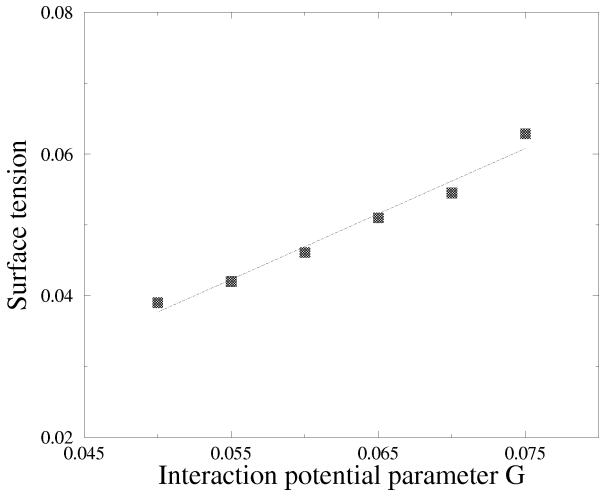

Figure 3. Evaluation of surface tension for two-phase flow.

2.3. Evaluation of fluid physical properties in the LB method

In the LB method, the fluid density and kinematic viscosity can be simulated directly. The surface tension of fluid in two-phase flow can be evaluated from the interaction potential G_σ [4]. *Figure 3* shows the simulation results of surface tension for different interaction potential parameters by the LB method. In the calculation, the lattice number is 51×51, the density is assumed to be similar in two fluids. The dependence of surface tension on the interaction potential G_σ is nearly linear in this model.

The contact angle of bubble interface on a solid surface depends not only on the fluid properties, but also on the fluid–solid interface. In a previous work [7], it has been shown that the static contact angle of two phases in the pool can be reasonably well predicted by equation (14) of [5]. By measuring the contact angle in the density distribution figure, obtained from the LB simulation with the 41×81 lattice, it is found in the present work that the static contact angle is a linear function of the fluid–solid interaction parameter G_t (*figure 4*). In this case, densities and the relaxation time are set to 1 for both fluids. For $G_\mathrm{t} = 0$ the solid surface is totally wettable by both fluids. In contrast, a zero contact angle indicates that the solid surface becomes unwettable by one of the fluids. In general, a bigger contact angle is predicted for the fluid with larger surface tension coefficient ($\sigma \sim G_\sigma$) (*figure 4*).

Successful applications of the FlowLab code and model to two-phase flows with accounting for surface

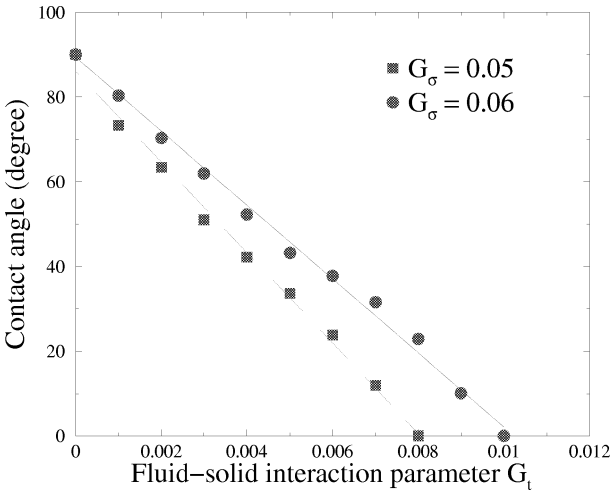

Figure 4. Evaluation of contact angle of two-phase flow in a pool.

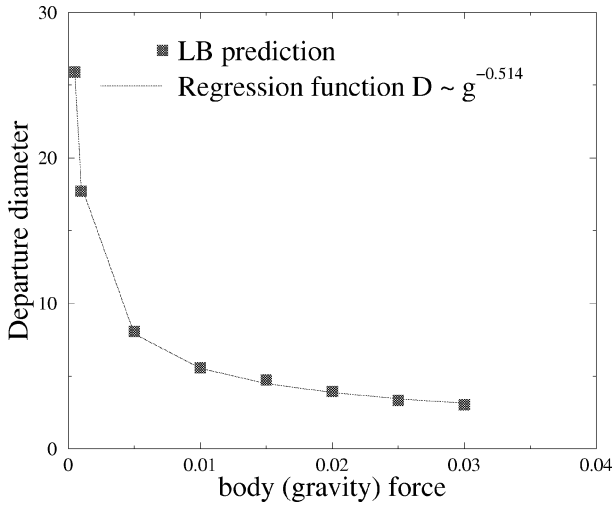

Figure 5. The body (gravity) force effect on bubble departure diameter, $G_\sigma = 0.06,\ G_t = 0.005,\ v = 0.1$.

tension and wettability were reported in [7] and [8]. Note that all the parameters and physical symbols in the LB simulation are nondimensional.

3. BUBBLE GROWTH AND DETACHMENT

This section presents the results of LB simulation for single bubble growth and detachment from a nozzle on a horizontal surface. The bubble detachment diameter is measured from results of simulations performed for different values for body force (gravity), surface tension and wettability (contact angle). The calculated results were then analyzed and compared to experimental and theoretical dependences of the bubble departure diameter. Excellent agreement between the calculated results and the experimental dependences was achieved, which serves as the basic validation for the two-phase flow-modeling method and code employed in further simulations.

Generally, when a bubble forms at the horizontal solid surface, its growth characteristics and time of detachment depend on both liquid–solid interface condition (wettability effect) and the balance of forces, which include gravity (body force), surface tension, and inertial force of gas injection.

The most widely used correlation for the departure diameter D_d of bubble on the horizontal surface is that proposed by Fritz [9] in which the bubble departure was determined by a balance between the buoyancy and surface tension forces acting normal to the solid surface. Based on his experimental measurement of the departure diameter over a range of pressures and on observation of the influence of the bubble growth rate on the departure diameter, Staniszewski [10] modified the Fritz equation to obtain the departure diameter correlation

$$D_\mathrm{d} = 0.0071\beta\left(\frac{2\sigma}{g\Delta\rho}\right)^{1/2}\left(1 + 34.3\frac{\partial D}{\partial t}\right) \qquad (20)$$

where $\partial D/\partial t$ is the bubble growth rate, which increases with the gas flow rate Q.

3.1. Effect of the body (gravity) force

Effect of the body (gravity) force on the bubble growth and detachment has recently received significant attention owing to the emerging interest in boiling heat transfer under microgravity conditions. In the literature, it was established that the bubble departure diameter is proportional to the inverse square root of the gravitational acceleration coefficient $D \sim g^{-1/2}$ (equation (20)). However, most of related experiments were terrestrial. It is therefore of interest to evaluate this dependence for a wide range of the gravity coefficient. *Figure 5* depicts LB simulation results. The bubble departure diameter calculated for different gravity forces was fit into a function of the form $D \sim g^{-0.514}$. This result is in a very good agreement with the previous theoretical and experimental correlations. It should be noted that at low gravity conditions, the relative role of surface tension and wettability on the bubble departure diameter increases.

Figures 6 and *7* show essentially similar behavior of bubble growth calculated for two different body forces.

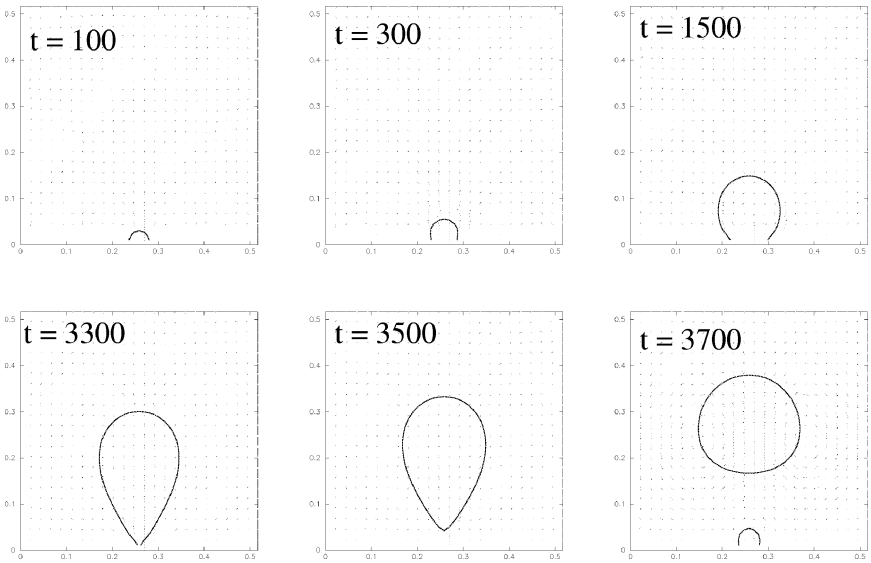

Figure 6. History of bubble growth and detachment for relatively low body (gravity) force, $G_\sigma = 0.06,\ g = 0.001,\ Q = 0.125,\ G_\mathrm{t} = 0.005$.

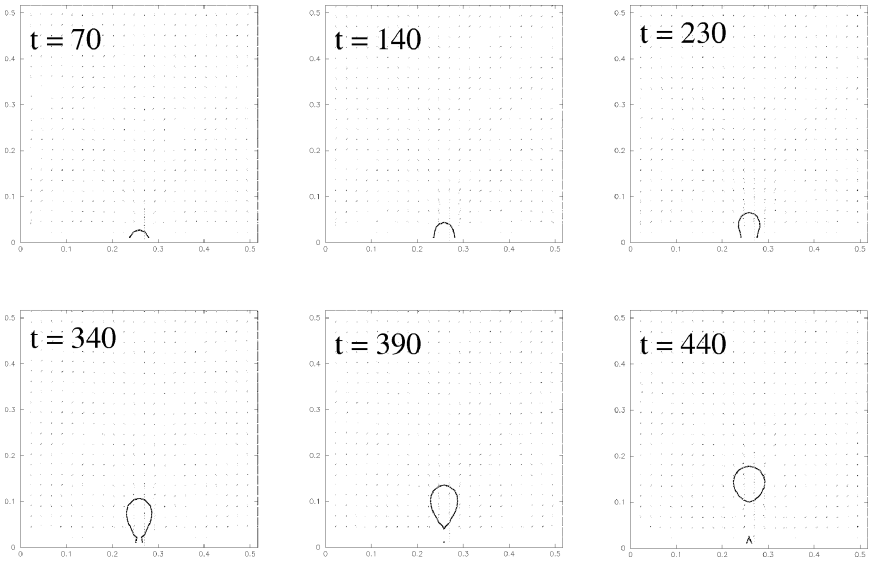

Figure 7. History of bubble growth and detachment for relatively high body (gravity) force, $G_\sigma = 0.06,\ g = 0.01,\ Q = 0.156,\ G_\mathrm{t} = 0.005$.

3.2. Effect of the surface tension

Figure 8 depicts results of LB simulations for different values of the surface tension coefficient. A regression function of the calculated bubble departure diameter depending on the fluid–fluid interaction potential has the form $D \sim G_\sigma^{1/2}$. Recalling results presented in *figure 3* regarding the linear relation between the surface tension coefficient σ and the fluid–fluid interaction potential G_σ, it can be concluded that the lattice-Boltzmann method employed is able to predict the well-known relation $D \sim \sigma^{1/2}$. The bubble departure diameter is thus smaller at elevated pressures since the surface tension is associated with the density gradient over the interface of contacting fluids.

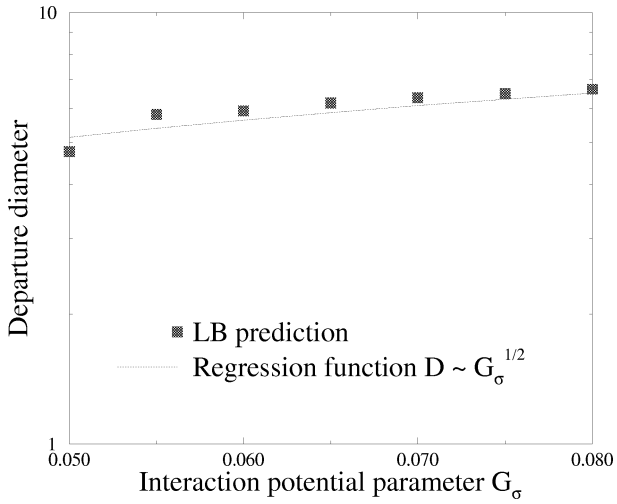

Figure 8. Surface tension effect on bubble departure diameter, $g = 0.01,\ v = 0.1,\ G_t = 0.005$.

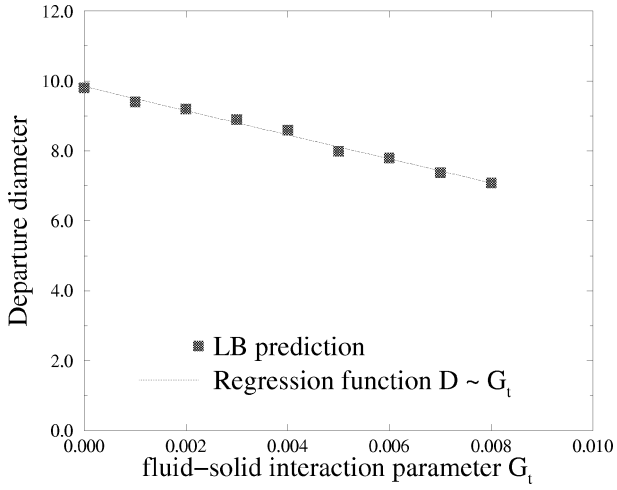

Figure 9. Wettability effect on bubble departure diameter, $g = 0.01,\ v = 0.1,\ G_\sigma = 0.06$.

3.3. Effect of the fluid wettability

The fluid wettability on a solid surface is a nanoscopic phenomenon, which has usually been quantified, macroscopically, in terms of the static contact angle at the triple fluid–fluid–solid join point. In the LB modeling, the wettability is implemented through the fluid–solid interaction potential G_t. *Figure 9* shows the linear dependence of the bubble departure diameter on the fluid–solid interaction potential, $D \sim G_t$. Taking into account the calculated results presented in *figure 4*, it can be concluded that the LB method is able to describe the linear relation between the bubble departure diameter and the static contact angle as previously established in experiments ($D \sim \beta$).

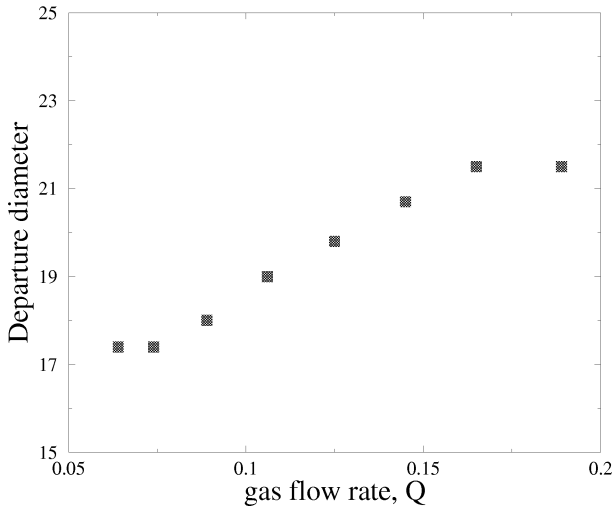

Figure 10. Flow rate effect on bubble departure diameter for relatively low body (gravity) force, $G_\sigma = 0.06,\ g = 0.001,\ G_t = 0.005$.

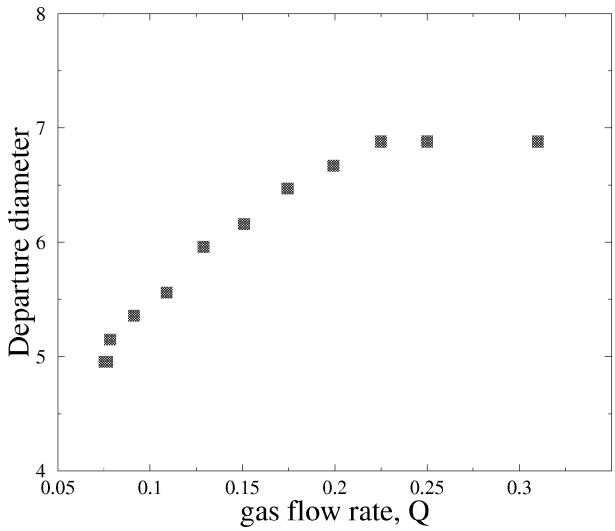

Figure 11. Flow rate effect on bubble departure diameter under relatively high body (gravity) force, $G_\sigma = 0.06,\ g = 0.01,\ G_t = 0.005$.

3.4. Effect of gas flow rate

Figures 10 and *11* show the bubble departure diameter calculated for two values ($g = 0.001$ and $g = 0.01$) of the body force. The dependence of the departure diameter on the flow rate Q can be seen in both cases.

In the intermediate range ($Q = 0.1-0.2$), the effect of the gas flow rate ($Q = 0.1-0.2$) on the bubble departure diameter is profound and can be evaluated, approximately, as $D \sim Q^{1/3}$ or $D \sim \partial D/\partial t$. This is in a good agreement with experimental data obtained, in the past, on bubble departure diameter in a wide range of gas injection rates. On one hand, it can be stated that such dependence reflects the correction required to the contact angle due to bubble growth inertia. On the other hand, it may simply indicate the need to consider the effect of the dynamic force balance during the fast bubble growth upon the bubble departure.

It was predicted that at both very low and very high gas flow rates, the bubble departure diameter appears to feature another dependence on the gas flow rate. At very high gas flow rates, the gas injection regime may well be in the jet mode, where surface tension governs the stability and breakup of the jet stream. Therefore, the bubble departure diameter remains constant for this range of the gas flow rate. At very small gas flow rates, the bubble growth inertia may be considered negligible.

We note here that the hydrodynamic behavior of a single gas bubble injected through a nozzle may be used as the first-order approximation model of a vapor bubble formed in the fully developed nucleate boiling regime. It has been established that, at heat fluxes close to CHF, boiling heat transfer is mainly governed by evaporation of the liquid microlayer in between the bubble and the heated surface [11]. As a result, the nucleate-boiling bubble growth is essentially driven by the vapor generation in the lowermost fraction of the bubble. More importantly, it is believed that the evaporation of microlayer and gas-phase addition mode hardly effect the bubble merging and coalescence investigated in the present work. It is because that actions of the bubble coalescence occur at a sufficient (macroscopic) distance from the location of the vapor generation or gas injection.

4. BUBBLE COALESCENCE CHARACTERISTICS

4.1. Bubble generated on a horizontal surface

4.1.1. Bubble coalescence in the vertical direction

Numerous experiments and analyses have been performed to study the phenomena of coalescence of bubbles produced from a single nozzle merged in a liquid pool. Under low gas flow rate condition, experiments show that the formation and detachment of distinct bubbles and their rise in a pool of water or in mineral oil is periodic [12]. With an increased gas flow rate, the bubbles start to rise in pairs. For high flow rates, members of a bubble pair interact with each other, forming a doublet. For even higher flow rates, the lower bubble often momentarily protrudes into the top bubble. Further increase in the flow rate causes the second bubble to penetrate the first one appreciably. In most cases, however, the two bubbles completely coalesce at a distance above the nozzle, yielding a single, large, irregular bubble. As the flow rate further increases, the coalescence takes place closer and closer to the orifice, until the bubbles coalescence occurs right at the nozzle exit. The same results were reported by Kyriakides et al. [13], who also proposed a classification of bubbling regimes into (i) single bubbling, (ii) pairing and single coalescence, (iii) double coalescence, (iv) triple bubble formation, (v) quadruple bubble formation, (vi) coalescence at the nozzle exit and triple or quadruple bubble formation, (vii) chaining and (viii) jet formation. It was observed that for a nozzle with diameter of 2 mm, the single coalescence occurs at a gas Reynolds number of 160.

Under nucleate boiling conditions, phenomena of bubble coalescence in the vertical direction may be significantly different from that observed in the case of the single nozzle. In particular, interaction of bubbles generated in neighboring nucleation sites may effect the bubble coalescence characteristics.

In the present work, the focus is placed on the multi-nucleation-site effect on the coalescence of bubble in the vertical direction. Bubble generation is simulated by injecting the gas through three nozzles merged in the liquid pool, using the FlowLab code.

Figure 12 shows the site distance effect on the bubble coalescence. For the case of $L = 17$ (L is the distance between the neighboring bubble generation sites, in lattice number), as the gas flow rate (the velocity at each nozzle entrance is set to 0.1) is relatively low, bubbles detached from each nozzle appear to behave independently. For the case of $L = 15$, the distance between neighboring detached bubbles is close enough to effect the liquid downward flow in between rising bubbles. In this counter-current two-phase flow regime, the interfacial drag force is sufficient to cause the rising bubble to slow down.

It is seen that the bubble coalescence is predicted to occur even when the second bubble has not fully developed at the nozzle site. The coalescence however ap-

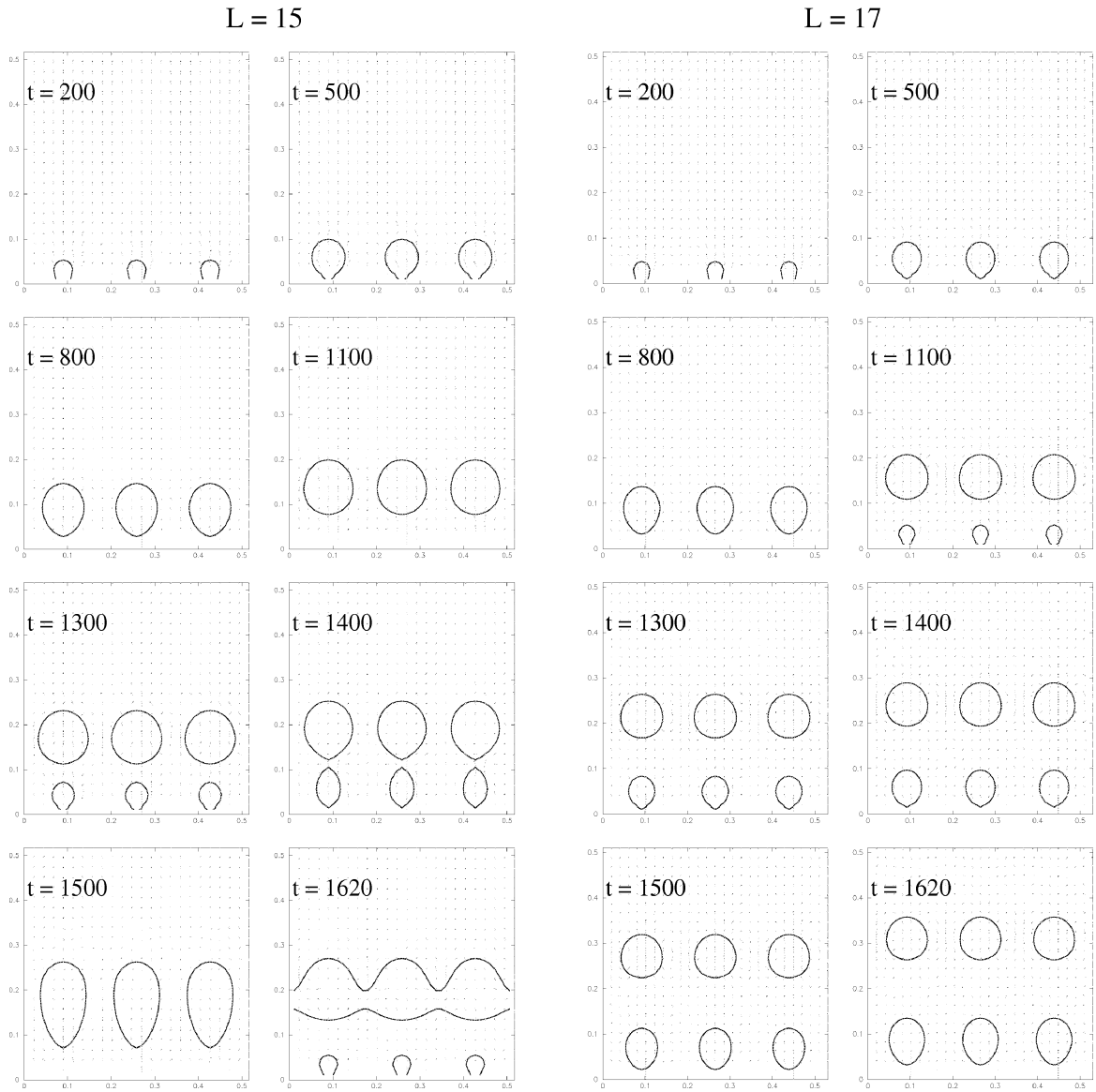

Figure 12. The effect of the distance between neighboring bubble generation sites on the vertical bubble coalescence ($g = 0.003,\ v = 0.1,\ G_\sigma = 0.06,\ G_t = 0.007$, lattice size is 45×90 for $L = 15$; 51×99 for $L = 17$).

pears to cause early detachment of the second bubble from the nozzle exit. Apparently, the surface tension force in this case is sufficient to overcome the adhesion of the bubble to the nozzle configuration. As a result, a large bubble is formed at some distance from the nozzle exit. Again, due to the surface tension, the bubble enlarges in its span, leading to a higher probability for neighboring bubbles to coalesce. These phenomena are predicted in the present LB simulation. Previously, this mechanism of bubble coalescence was observed in experiments [1] and was used to developed a theoretical model for CHF [14]. In this model a vapor layer at a distance from the heated surface is assumed to be responsible for causing the transition from nucleate boiling to film boiling. In fact, the formation of the vapor layer leads to a rapid evaporation of the liquid layer underneath the vapor layer, rendering a heat transfer crisis.

4.1.2. Bubble coalescence in the lateral direction

In a model for critical heat flux (CHF) proposed by Haramura and Katto [15] a macrolayer is assumed to form when vapor bubbles form, grow and coalesce prior to their detachment from the heated surface. A similar model developed by Liaw and Dhir [16] was found to successfully predict CHF on the vertical surface. The argument for these models is based on experimental observations that large mushroom bubbles with several stems form on the heater surface near CHF. Under nucleate boiling conditions, the nucleation site density increases with heat flux, and causes a higher frequency of bubble coalescence. The vapor bubble hovering over the heater surface becomes larger, with many stems feeding the vapor. As liquid replenishment is depleted under the center part of this vapor cloud, momentary dry patches begin to form. For this regime, the heat flux approaches the CHF [17].

The bubble coalescence in the lateral direction depends on the influence area of bubble, which is related to the bubble size and the hydrodynamics of the two-phase flow near the bubble region. *Figure 13* shows the simulation results of the LB method of the effect of bubble generation (nucleation) site density on the bubble coalescence behavior. In the case of a smaller distance between neighboring bubble generation sites, which represents the larger bubble generation site densities (the case of $L = 11$ in *figure 13*), the bubbles start to merge during the early stage of their growth, and eventually, the coalesced bubbles cover the surface. When the bubble generation site density decreases, the bubble coalescence is predicted to occur in a later stage of their growth (the case of $L = 15$ in *figure 13*). After bubble coalescence, the liquid stems form on the surface between neighboring bubble generation sites. With further decrease of the bubble generation site density (the case of $L = 17$ in *figure 13*), the bubbles remain discrete while departing the surface. They may still coalesce at a distance from the surface due to the motion of the bubbles and their deformation. However, at a low nucleation site density, the detachment and rising of bubbles are visually independent, although the liquid flow in between the bubbles remains affected by the distance between neighboring sites.

Parameters, such as body force (gravity), surface tension, wettability, and flow rate of gas generation, can affect the bubble influence area, which is related to the bubble departure size. The LB simulation results indicate that the effect of these parameters on the bubble coalescence is similar to that on the bubble departure size. From *figure 14*, it can be seen that smaller body force (gravity) causes earlier coalescence in the lateral direction. When the gravity is large enough, the bubbles will remain discrete during the whole process.

4.2. Bubbles generated on a vertical surface

In comparison with the study of dynamics of bubbles generated on the horizontal surface, less attention has been paid to the coalescence of bubbles generated on the vertical surface, even though the boiling heat transfer both in the vertical tubes and on the vertical surfaces have extensively been examined. Most of the past works on bubble behavior on the vertical surface employed small test section with few bubble generation sites (e.g., in [18] the heater size is 80 mm long and 40 mm in diameter, in [11] only four nozzles are employed). It has been shown that bubble behavior near CHF condition is significantly dependent on the bubble movement trajectory [11].

In the present LB simulation, three bubble generation sites are employed in the computational domain. However, setting the periodic boundary condition at both upper and lower sides of the domain enables simulation of the large surface area. The different bubble generation site density can be obtained by changing the distance between neighboring bubble generation site. *Figure 15* shows the results of LB simulation on the bubble coalescence behavior for the different bubble generation site densities. For the cases with larger bubble generation site density (the cases $L = 11$ and $L = 13$ in *figure 15*), the bubbles start to merge at their earlier stage of growth, then gas covers all the surface. When the bubble generation site density decreases (the case $L = 15$ in *figure 15*), the bubbles are coalesced at the later stage of their growth, the liquid stem forms between the two bubble generation sites. These behaviors are almost the same as those for the horizontal surface (e.g., *figure 13*). When the bubble generation site density decreases further, firstly, the bubbles are detached, move upward, then merge into the gas stem of bubble generation site at the upper position, forming a larger bubble. If the distance between the two bubble generation sites is not large enough, the coalesced large bubble may merge into one at the upper bubble generation site. As a result, it forms a big mushroom with liquid stems (the case $L = 17$ in *figure 15*).

Figure 16 shows the LB simulation results on the bubble coalescence behavior on the vertical surface under different body force (gravity) condition. For the case

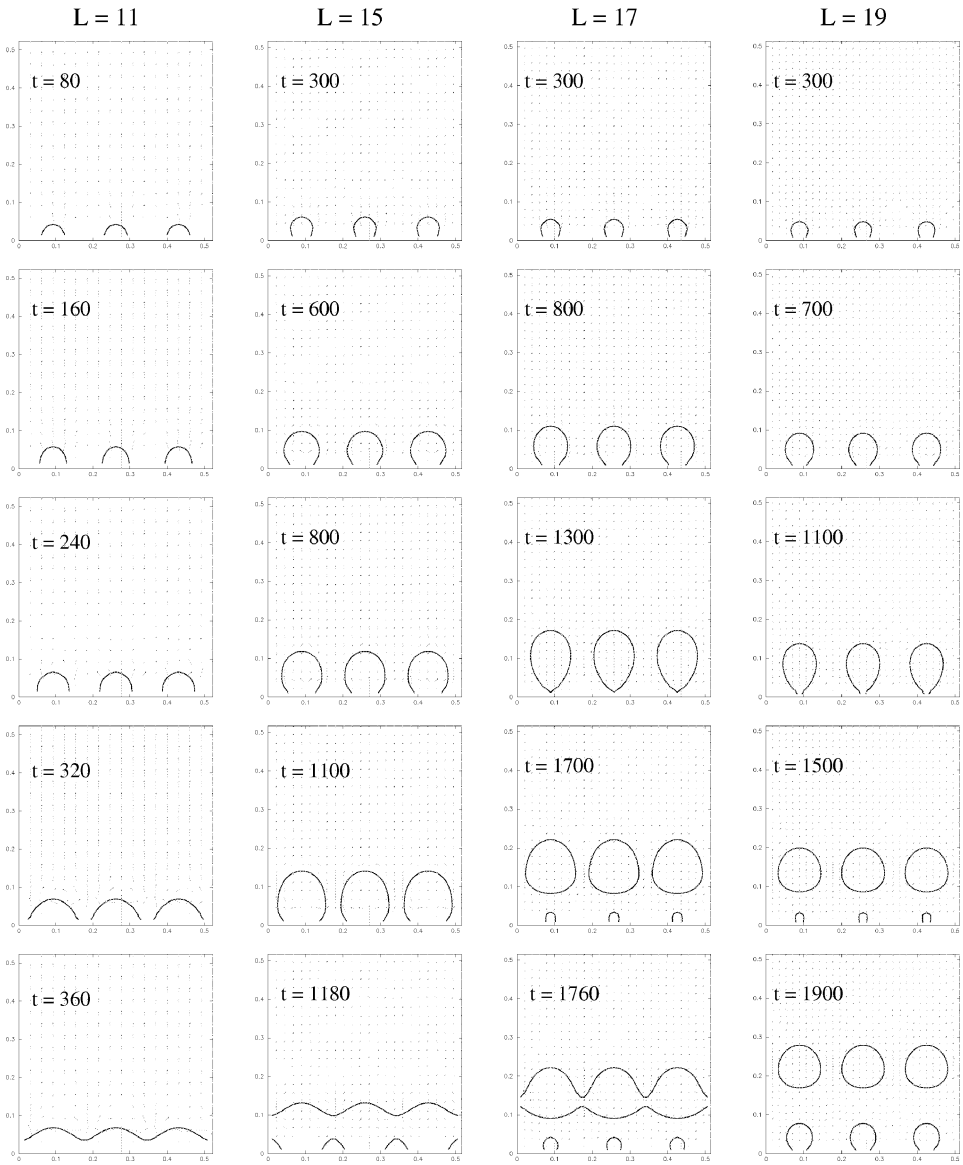

Figure 13. The lateral bubble coalescence behavior for different distances between neighboring bubble generation sites on the horizontal surface ($g = 0.003,\ v = 0.1,\ G_\sigma = 0.06,\ G_t = 0.005$, lattice size is 33×66 for $L = 11$; 45×90 for $L = 15$; 51×99 for $L = 17$; 57×114 for $L = 19$).

with lower body force (gravity) (e.g., the case $g = 0.005$ in *figure 16*), the bubble coalescence occurs before the bubbles are detached from their generation sites. If the body force (gravity) is large enough, the bubble will be detached with small size. The detached bubbles move upward, then merge into the gas stem at the their upper bubble generation site. Larger bubbles form, and are detached again. After their second coalescence, the coalesced bubbles may detach again. As a result of the coalescence process, the surface may become fully covered by gas layer (the case $g = 0.005$ in *figure 16*).

4.3. Coalescence of bubbles generated on an inclined downward-facing surface

According to the experimental results on the effect of inclination of heater surface on the boiling curve [19], the

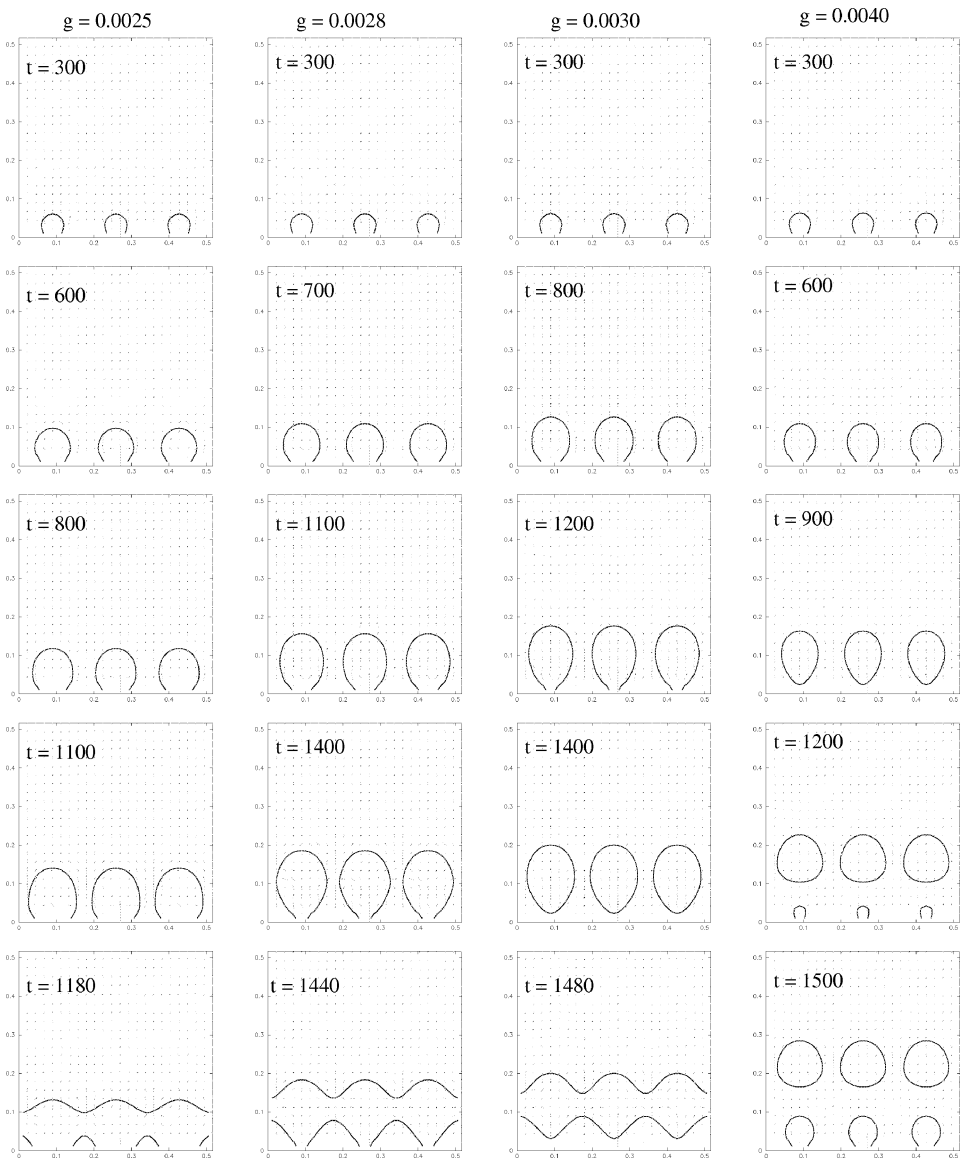

Figure 14. The lateral bubble coalescence behavior on the horizontal surface under different the body (gravity) forces ($\upsilon = 0.1$, $G_\sigma = 0.06$, $G_t = 0.005$, lattice size is 45×90).

partial nucleate-boling heat fluxes are generally higher on a downward-facing surface, but in fully developed nucleate boiling the surface orientation has little effect. It is because in the partial nucleate boiling regime the heater inclination can significantly effect the convective heat flux, so the total heat flux. However, experimental results [20] revealed that the CHF increases with the inclination angle of the downward-facing heater surface. It is believed that the bubble trajectory on the inclined downward-facing heater surface is effected significantly because of the different magnitudes and directions of gravity force for different inclination angles of heater surface.

Figure 17 presents the LB simulation results on the bubble coalescence behavior on the downward-facing surface with different inclination angles α. The inclination angle α is reflected in *figure 17* through the direction of body force (gravitational acceleration) related to the

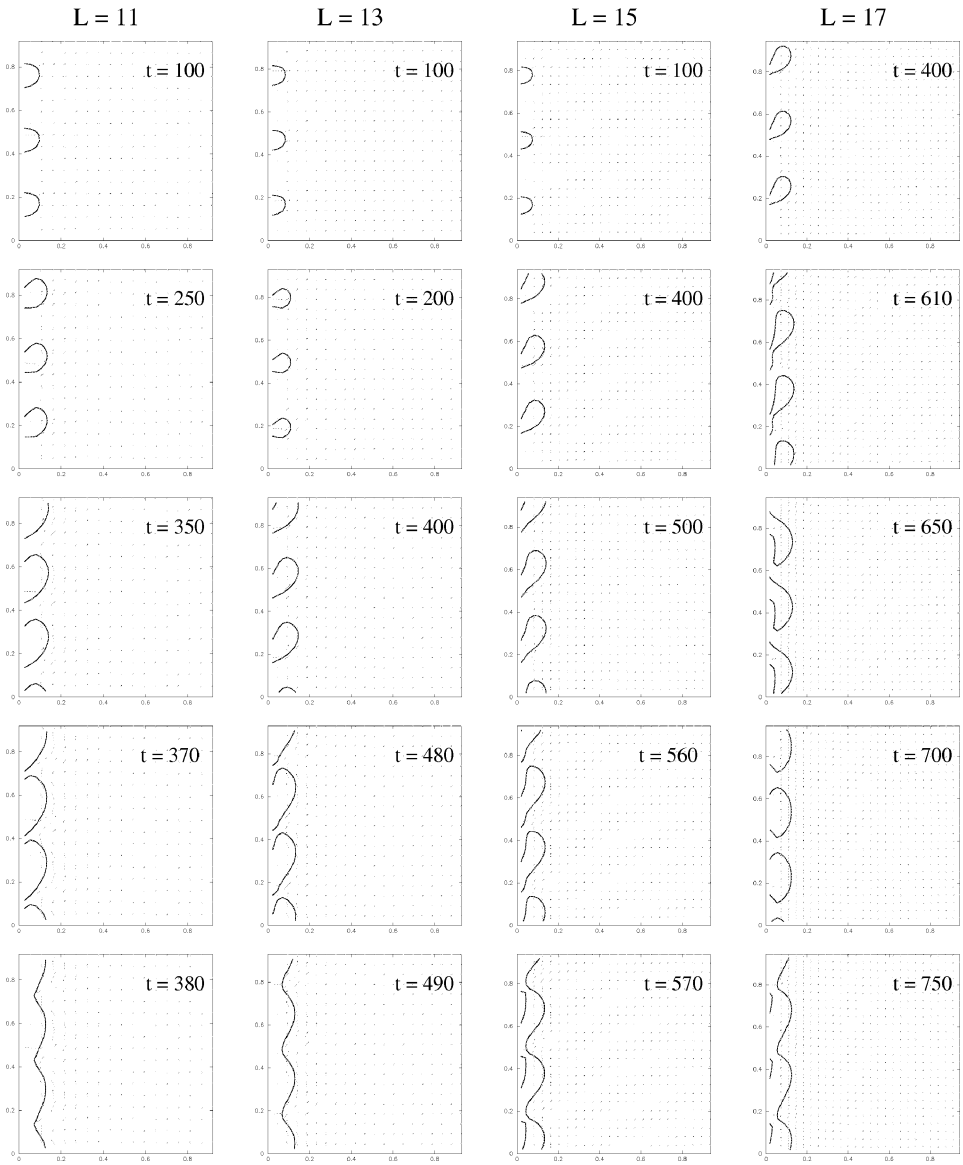

Figure 15. The bubble coalescence behavior on the vertical surface for different distances between neighboring bubble generation sites ($g = 0.005,\ v = 0.1,\ G_\sigma = 0.06,\ G_t = 0.01$, lattice size is 38×33 for $L = 11$; 44×39 for $L = 13$; 50×45 for $L = 15$; 56×51 for $L = 17$).

bubble generation surface, which faces downward. It can be seen from *figure 17* that for the cases with smaller inclination angle α, as the magnitude of body force (gravity), which acts on the bubble at its moving direction, is smaller, bubbles tend to stay longer at the generation site. As a result, bubble's influence area is smaller, which delays the bubble coalescing. As the inclination angle α of surface increases, the bubble influence area becomes larger in both growth and detachment stages, so that the bubbles tend to merge earlier. However, if the inclination angle α is close to 90 degrees (vertical), the bubbles may be detached, but then merge into another bubble generating at a site downstream.

In general, it is found that the LB simulation results correctly reflects the tendency of dependence of CHF on the inclination angle of the downward-facing surface.

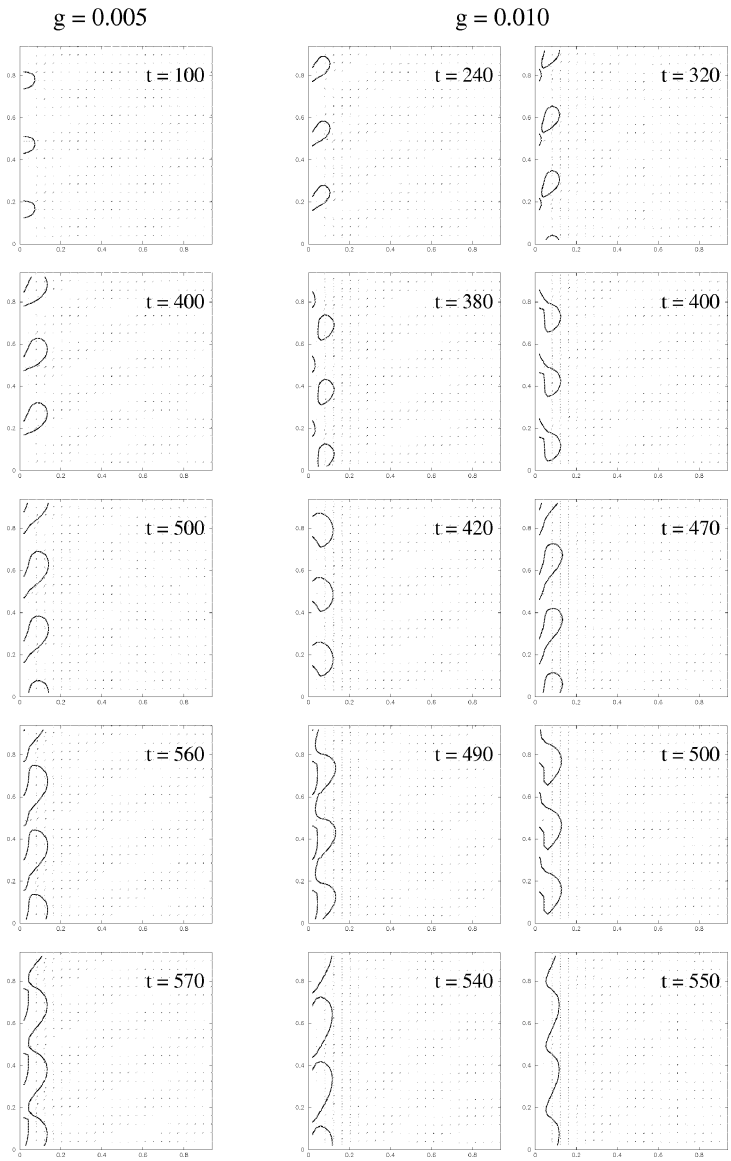

Figure 16. The bubble behavior on the vertical surface under different body (gravity) force conditions ($v = 0.1,\ G_\sigma = 0.06,\ G_t = 0.01$, lattice size is 45×50 and $L = 15$).

5. SUMMARY

In the present work, the FlowLab code, based on the D2Q9 lattice Boltzmann model for two-phase flow, is employed to simulate the behavior of bubble coalescence dynamics on vertical, horizontal and inclined downward-facing surfaces.

Within the current limitations of the lattice-Boltzmann technique in handling fluid pairs with significant difference in physical properties, it was found that this approach provides a realistic picture of the single and multiple bubble behavior. In particular, analysis of the LB simulation results revealed that the major parametric dependencies of the bubble departure diameter on various physical parameters (body force) and physical properties (surface tension, wettability) are correctly predicted. The bubble departure diameter of bubbles on the horizontal surfaces, calculated by the LB simulation, was found in

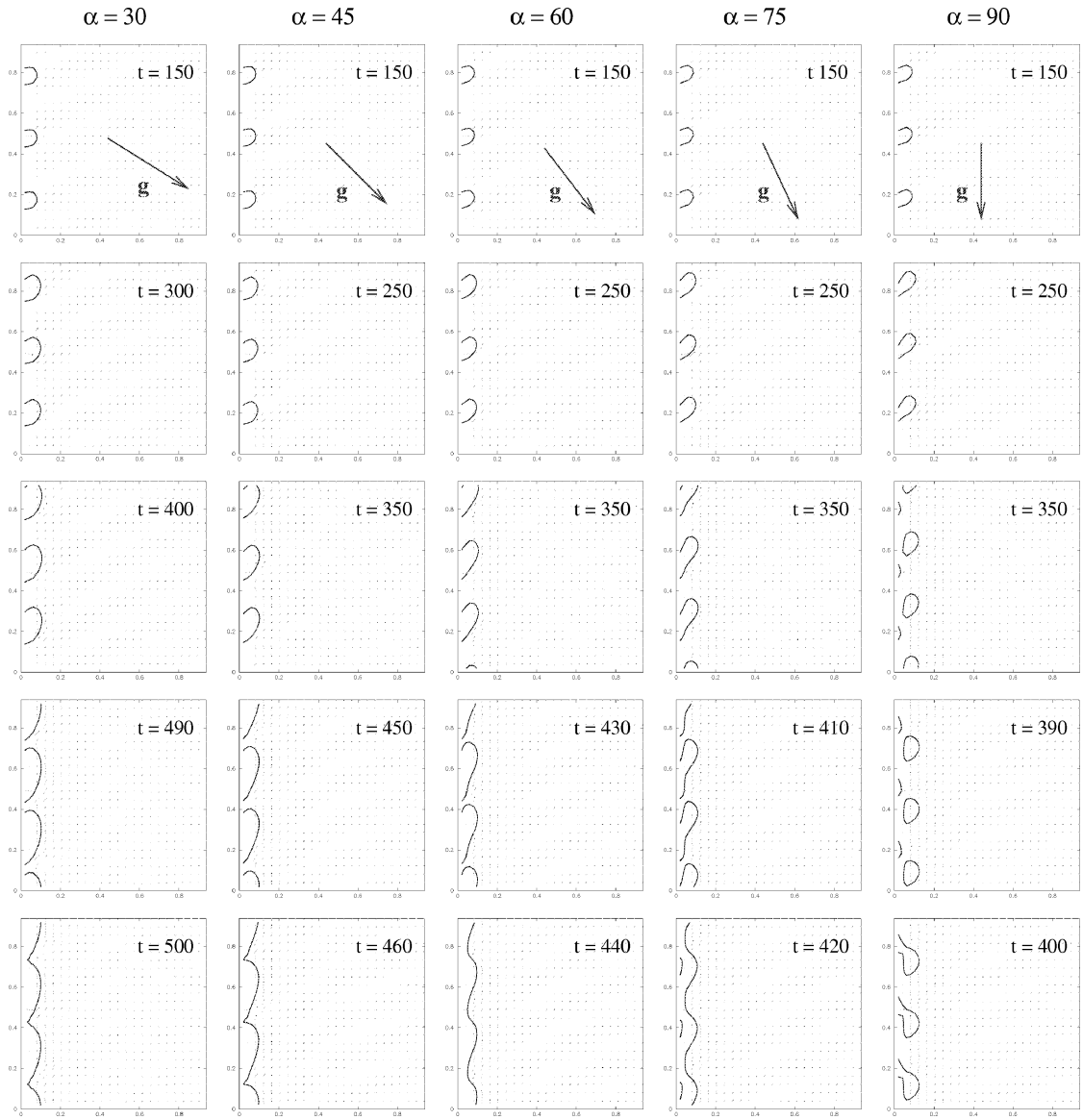

Figure 17. The effect of inclination angle of surface on the bubble behavior ($g = 0.01,\ v = 0.1,\ G_\sigma = 0.06,\ G_\mathrm{t} = 0.01$, lattice size is 45×50 and $L = 15$).

excellent agreement with experimentally established dependences.

Hydrodynamic aspects of bubble coalescence are investigated by simulating the growth and detachment behavior of multiple bubbles generated by the nozzles on different surfaces. It was observed that not only the bubble generation (nucleation) site density but also the surface position have a profound effect on the bubble coalescence characteristics. For cases with downward-facing surfaces ($\alpha < 90^\mathrm{o}$), the friction between the bubbles and the wall boundary appears to lead to significantly large size of bubbles before enabling their upward slipping motion. Apparently, this behavior is responsible for an earlier bubble coalescence, and therefore, lower values of maximum heat removal rates, in a similar nucleate boiling regime on a downward-facing surface. Multiple coalescence was predicted on the vertical surface as the bub-

ble detached from a lower elevation merges with the bubble forming on a higher site.

More interestingly, three distinct regimes of bubble coalescence were predicted in the LB simulation: lateral coalescence of bubbles situated on the surface; vertical coalescence of bubbles detached in a sequence from a site; and lateral coalescence of bubbles, detached from the surface. These three regimes were predicted at different combinations of governing parameters and properties. In fact, observations of all three regimes in boiling experiment were reported. These observations then served as fundamental hypotheses for different models [2, 21, 22] of critical heat flux in pool boiling on horizontal surfaces.

It should be noted that the present work was performed to explore the capability and limitation of the lattice-Boltzmann method, in general, and the FlowLab code, in particular, for multiphase-flow modeling. The encouraging results of the present study serve as a starting point for a continued study on boiling regime transition by means of the lattice-Boltzmann method.

Acknowledgements

This work was supported by the Swedish Nuclear Power Inspectorate, the US Nuclear Regulatory Commission, Swedish and Finish Power Companies, Nordic Nuclear Safety Project and Swiss Nuclear Inspectorate.

REFERENCES

[1] Gaertner R.F., Photographic study of nucleate pool boiling on a horizontal surface, ASME J. Heat Transfer 87 (1965) 17–29.

[2] Dhir V.K., Nucleate and transition boiling heat transfer under pool and external flow conditions, Int. J. Heat and Fluid-Flow 12 (4) (1991) 290–314.

[3] Qian Y.H., D'Humieres D., Lallemand P., Lattice BGK models for Navier–Stokes equation, Europhys. Lett. 17 (6) (1992) 479–484.

[4] Shan X., Chen H., Lattice Boltzmann model for simulating flows with multiple phases and components, Phys. Rev. E 47 (1993) 1815–1819.

[5] Martys N.S., Chen H., Simulation of multicomponent fluids in complex three-dimensional geometries by the lattice Boltzmann method, Phys. Rev. E 53 (1996) 743–750.

[6] Shan X., Doolen G., Diffusion in a multicomponent lattice Boltzmann equation model, Phys. Rev. E 54 (1996) 3614–3620.

[7] Yang Z.L., Nourgaliev R.R, Dinh T.N., Sehgal B.R., Investigation of two-phase flow characteristics in a debris particle bed by a Lattice-Boltzmann model, in: 2nd International Symposium on Two-phase Flow Modelling and Experimentation, Pisa, Italy, May 23–25, 1999.

[8] Nourgaliev R.R., Dinh T.N., Sehgal B.R., Numerical simulation of droplet deformation and break-up by a lattice-Boltzmann method, in: CD-ROM Proceedings of the Third International Conference on Multiphase Flow 98, Lyon, France, 1998.

[9] Fritz W., Maximum volume of vapor bubbles, Physik Zeitschr. 36 (1935) 379–384.

[10] Staniszewski B.E., Nucleate boiling bubble growth and departure, MIT Tech. Rep. No. 16, Cambridge, MA, 1959.

[11] Katto Y., Otokuni S., Behavior of vapor masses on a vertical flat surface of comparatively large height near critical heat flux conditions in saturated pool boiling, Int. J. Heat Mass Tran. 37 (Suppl. 1) (1994) 255–263.

[12] Davidson L., Amic E., Formation of gas bubbles at horizontal orifices, AIChE J. 2 (1956) 337–342.

[13] Kyriakides N.K., Kastrinakis E.G., Nychas S.G., Bubbling from nozzles submerged in water: transitions between bubbling regimes, Can. J. Chem. Engrg. 75 (1997) 684–691.

[14] Hsu Y.Y., Graham R.W., Transport processes in boiling and two-phase system including near-critical fluid, American Nuclear Society, Inc., 1986.

[15] Haramura Y., Katto Y., A new hydrodynamic model of critical heat flux, applicable widely to both pool and forced convection boiling on submerged bodies in saturated liquids, Int. J. Heat Mass Tran. 26 (1983) 389–399.

[16] Liaw S.P., Dhir V.K., Void fraction measurements during saturated pooling boiling of water on partially wetted vertical surfaces, Trans. ASME, J. Heat Transfer 111 (1989) 731–738.

[17] Kirby D.B., Westwater J.W., Bubble and vapor behavior on a heated horizontal plate during pool boiling near burnout, Chem. Engrg. Prog. Symp. Ser. 61 57 (1965) 238–248.

[18] Ishigai S., Kuno T., Experimental study of transition boiling on a vertical wall in open vessel, Bull. JSME 9 (1966) 361–368.

[19] Nishikawa K., Fujita Y., Ohta H., Effect of surface configuration on nucleate boiling heat transfer, Int. J. Heat Mass Tran. 27 (1974) 1559–1571.

[20] Theofanous T.G., Syri S., Salmassi T., Kymalainen O., Tuomisto H., Critical heat flux through curved, downward facing, thick walls, Nuclear Engineering and Design 151 (1994) 247–258.

[21] Zuber N., Hydrodynamic aspects of boiling heat transfer, Ph.D. Thesis, University of California, Los Angeles, 1959.

[22] Tong L.S., Boiling Heat Transfer and Two-Phase Flow, John Wiley, New York, 1975.